

Research Article

Open Access



# Tailoring the microstructure of lead-free KNN piezoelectric ceramics for force-sensitive smart windows

Jinfeng Lin<sup>1,#</sup>, Jianlin Peng<sup>1,#</sup>, Xiangyu Huang<sup>1</sup>, Qifa Lin<sup>2</sup>, Peng Li<sup>3</sup>, Xiao Wu<sup>2</sup>, Zhen Yang<sup>1</sup>

<sup>1</sup>Strait Institute of Flexible Electronics (SIFE, Future Technologies), Fujian Key Laboratory of Flexible Electronics, Fujian Normal University and Strait Laboratory of Flexible Electronics (SLoFE), Fuzhou 350117, Fujian, China.

<sup>2</sup>Institute of Advanced Ceramics, College of Materials Science and Engineering, Fuzhou University, Fuzhou 350108, Fujian, China.

<sup>3</sup>School of Materials Science and Engineering, Liaocheng University, Liaocheng 252059, Shandong, China.

#Authors contributed equally.

**Correspondence to:** Assoc. Prof. Peng Li, School of Materials Science and Engineering, Liaocheng University, Liaocheng 252059, Shandong, China. E-mail: pengli@lcu.edu.cn; Prof. Zhen Yang, Strait Institute of Flexible Electronics (SIFE, Future Technologies), Fujian Key Laboratory of Flexible Electronics, Fujian Normal University and Strait Laboratory of Flexible Electronics (SLoFE), Fuzhou 350117, Fujian, China. E-mail: ifezhyang@fjnu.edu.cn

**How to cite this article:** Lin, J.; Peng, J.; Huang, X.; Lin, Q.; Li, P.; Wu, X.; Yang, Z. Tailoring the microstructure of lead-free KNN piezoelectric ceramics for force-sensitive smart windows. *Microstructures* 2025, 5, 2025058. <https://dx.doi.org/10.20517/microstructures.2024.182>

**Received:** 27 Dec 2024 **First Decision:** 12 Mar 2025 **Revised:** 30 Mar 2025 **Accepted:** 8 Apr 2025 **Published:** 27 Apr 2025

**Academic Editor:** Dawei Wang **Copy Editor:** Fangling Lan **Production Editor:** Fangling Lan

## Abstract

Ferro/piezoelectric transparent materials with both excellent piezoelectricity and transparency are of great interest for irreplaceable applications in numerous fields such as photoacoustic imaging and transparent robots. Nevertheless, developing a lead-free ferroelectric ceramic that meets both distinct transparency and high piezoelectricity has always been challenging. Herein, the simple single Sm<sup>3+</sup> doped KNN ferroelectric ceramics (xSm) are designed to improve transparency and achieve reasonable piezoelectricity. The results indicate that although the donor doping effect of Sm<sup>3+</sup> significantly improves the transparency by mainly causing grain refinement and densification improvement, it also enhances the relaxor behavior of KNN ceramics and weakens the piezoelectricity. Despite this, with proper Sm doping, reasonable piezoelectricity can still be achieved in the xSm transparent ceramics without causing a significant decrease in Curie temperature. Ultimately, excellent comprehensive performance was achieved in the 1.0 Sm ceramic ( $T_{-65\%}$  at 900 nm,  $T_C$ ~395 °C,  $d_{33}$ ~65 pC/N), competitively in the KNN-based transparent ceramics. In force sensitivity testing, the 1.0 Sm ceramic also exhibits prominent force response electrical output characteristics, which is expected to be applied in smart windows that require real-time pressure detection. This work furnishes a methodology for the fabrication of KNN-based



© The Author(s) 2025. **Open Access** This article is licensed under a Creative Commons Attribution 4.0 International License (<https://creativecommons.org/licenses/by/4.0/>), which permits unrestricted use, sharing, adaptation, distribution and reproduction in any medium or format, for any purpose, even commercially, as long as you give appropriate credit to the original author(s) and the source, provide a link to the Creative Commons license, and indicate if changes were made.



transparent piezoceramics, while contemporaneously recommending innovative perspectives for broadening their range of applications.

**Keywords:** Transparency, lead-free, KNN-based, piezoelectricity, smart window

## INTRODUCTION

Following the heightened emphasis on environmental protection and energy conservation, substantial progress has been achieved in the reasonable utilization of energy and the development of energy-saving products. Within this context, electrochromic materials were first designed for application in energy-saving lighting automatic control systems, including buildings, cars, and aerospace, forming “smart windows” that can adjust the transmittance of solar radiation in real time. Subsequently, smart windows related to photochromism and thermochromism gradually emerged<sup>[1-5]</sup>. Actually, in addition to windows with intelligent color regulation, windows that can intelligently sense signals such as temperature and force in the surrounding environment without changing their transparency are also urgently needed products in the high-tech era.

Owing to the unique combination of transparency, mechanical strength, and ferroelectric/piezoelectric/dielectric properties, transparent ferro/piezoelectric materials can be used not only in traditional energy harvesters, ultrasonic transducers, and microdisplacements<sup>[6]</sup>, but also show great developmental advantages and potentials in high-tech photoacoustic imaging sensors, electro-optical devices, transparent robots, and even force-sensitive smart windows<sup>[7-10]</sup>. The PMN-PT crystals are representative ferro/piezoelectric transparent materials. Although their transparency is relatively poor because of their complex and disordered domain structure, they have attracted massive attention for their high piezoelectricity near the morphotropic phase boundaries (MPBs)<sup>[11,12]</sup>. In 2020, Qiu *et al.* showed that for the rhombohedral PMN-PT crystals with [001] orientation, repeated polarization by alternating-current (AC) electric fields can effectively eliminate the light scattering from 71° domain walls, achieving both near-saturation optical transmittance and ultrahigh piezoelectricity<sup>[13]</sup>. Nevertheless, considering the difficulty of preparing single-crystal materials and the human health issues caused by the toxicity of lead, the development of low-cost and high-performance lead-free environmentally friendly ferro/piezoelectric transparent polycrystalline ceramics is urgently needed<sup>[14,15]</sup>.

The influence on the optical transmittance of ceramics can be generally summed up as following aspects<sup>[16,17]</sup>. Firstly, powders with high purity, uniform particle size distribution, and appropriate pre-sintering temperature are prerequisites for preparing transparent ceramics. Secondly, in order to minimize light scattering losses, it is necessary to prevent the formation of obvious impurity phases, macroscopic pores and defects inside the ceramic. Suitable doping concentrations, as well as optimal heating/cooling rates, sintering temperature, and holding time, are crucial for achieving high-density and pure-phase ceramics during sintering. Additionally, the light scattering theory suggests that when the scale of the scattering center is equivalent to the wavelength of the incident light, it will result in the strongest scattering and weakest optical transmittance. Hence, regulating grain size to deviate from the wavelength range of incident light has been widely used to ameliorate the optical transmittance of ceramics in the visible light region. Last but not least, the surface roughness of ceramics also directly affects their optical transmittance, so the surface treatment needs to be carried out by polishing technology to more accurately reflect the true transparency of the sample. To date, potassium sodium niobate ( $\text{K}_{0.5}\text{Na}_{0.5}\text{NbO}_3$ , KNN)-based ceramics are the most promising candidates for the preparation of high-transparency functional ceramics and have been extensively studied in comparison with other representative lead-free ferro/piezoceramics, such as bismuth

sodium titanate (BNT)-based, barium titanate (BT)-based, and bismuth ferrite (BiFeO<sub>3</sub>)-based ceramics<sup>[15-17]</sup>.

The transparency of  $(1-x)\text{K}_{0.5}\text{Na}_{0.5}\text{NbO}_3-x\text{SrTiO}_3$  ceramics was first discovered and reported by Kosec *et al.* as early as 2004<sup>[18]</sup>, but it was not until 2008 that KNN-based transparent ceramics gradually attracted people's attention<sup>[15-17,19]</sup>. For example, Li *et al.* reported the Li/Bi comodified KNN-based ceramics with high optical transmittance of 60%-70% (near-IR region) and considerable electro-optic response (120-200 pm/V)<sup>[20,21]</sup>. Qu *et al.* found that the  $0.8\text{K}_{0.5}\text{Na}_{0.5}\text{NbO}_3-0.2\text{Sr}(\text{Sc}_{0.5}\text{Nb}_{0.5})\text{O}_3$  ceramics exhibits both high optical transmittance (~60% at 700 nm) and high recoverable capacitive energy storage ( $W_{\text{rec}} \sim 2.48 \text{ J/cm}^3$ )<sup>[22]</sup>. Meanwhile, through component design and conventional solid-state reaction method, we have also successfully prepared several KNN-based ferroelectric transparent ceramics, such as Er-KNN-BST and La/Er KNN<sup>[5,15]</sup>, which exhibit superior optical transmittance (> 70% at 900 nm) and significant photochromic contrast ( $\Delta R > 60\%$ ). It is worth noting that there is not only a trade-off between piezoelectricity and Curie temperature in KNN-based ferro/piezoceramics, but also between piezoelectricity and transparency. For instance, high transparency KNN-based ceramics typically exhibit fine grain sizes, relaxor nano/microdomains, and high-symmetric pseudo-cubic phase, as opposed to the large grain sizes, long-range ordered domain structures, and low-symmetric anisotropic phase required for the conventional KNN-based ceramics with superior piezoelectricity, leading to a weak piezoelectric response. Therefore, the simultaneous realization of superior piezoelectricity, high Curie temperature ( $T_C$ ), and desired transparency in KNN-based ferro/piezoceramics is currently a great challenge.

Rare-earth (RE) ion doping is an extremely effective strategy for optimizing both optical transmittance and electrical properties in KNN-based ferro/piezoceramics. Here,  $x \text{ mol\% Sm}^{3+}$ -doped  $\text{K}_{0.5}\text{Na}_{0.5}\text{NbO}_3$  (abbreviated as  $x\text{Sm}$ ) ferroelectric transparent ceramics with simultaneously superior transparency, high Curie temperature, and reasonable piezoelectricity were successfully developed via the simple single RE ion doping strategy, and their optical/electrical properties and the multidimensional microstructure were also systematically studied. After appropriate Sm doping, the  $x\text{Sm}$  ceramics possess a dense structure, finer grain size, more highly symmetric pseudo-cubic phase, and higher bandgap, thereby demonstrating prominent transparency. It is worth noting that although the doping of Sm also enhances the relaxor behavior of KNN ceramics and weakens the piezoelectricity, reasonable piezoelectricity can still be obtained in the  $x\text{Sm}$  transparent ceramics with appropriate Sm doping, while not significantly affecting the Curie temperature. Ultimately, high transparency, high Curie temperature, and good piezoelectricity were simultaneously achieved in the 1.0 Sm ceramic. Leveraging the piezoelectric effect, the 1.0 Sm transparent ceramic was developed to exhibit excellent circulative electrical signal output characteristics under low pressure, demonstrating outstanding force response behavior. This innovation conceptualizes the application of smart windows that require real-time pressure detection [Figure 1].

## MATERIALS AND METHODS

**Sample preparation:** A series of  $x \text{ mol\% Sm}^{3+}$ -doped  $\text{K}_{0.5}\text{Na}_{0.5}\text{NbO}_3$  ( $0 \leq x \leq 3$ , abbreviated to  $x\text{Sm}$ ) ceramics were prepared via conventional solid-state reaction method and pressureless sintering with high-purity raw materials, including  $\text{Na}_2\text{CO}_3$ ,  $\text{K}_2\text{CO}_3$ ,  $\text{Nb}_2\text{O}_5$ , and  $\text{Sm}_2\text{O}_3$ . The powder mixtures weighed according to the formula were first ball milled with ethyl alcohol and  $\text{ZrO}_2$  balls for 12 h, then successively dried and calcined (850 °C/4 h). After being ball-milled again for 12 h and dried, the calcined powders were granulated through the 6 wt% polyvinyl alcohol (PVA) aqueous adhesive, and then pressed under uniaxial pressure of 200-300 MPa to make a disc with a diameter of 12 mm and a thickness of 1 mm. Subsequently, after binder removal at 800 °C, the discs were sintered at 1,160-1,170 °C for 6 h to achieve densification. In the end, the high-quality ceramics prepared were thinned/polished to a certain thickness to test the optical and electrical properties.

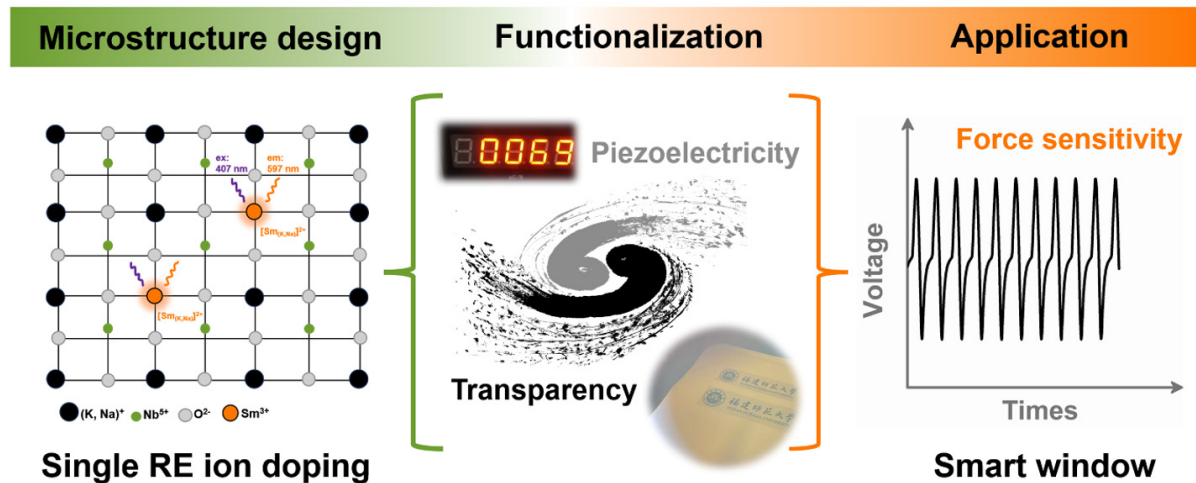


**Figure 1.** Schematic illustration of the microstructure design and application concept for the  $x\text{Sm}$  transparent ferro/piezoelectric ceramics.

**Characterization:** UV-Vis-IR spectroscopy (PerkinElmer Lambda 950) was used to characterize the optical transmittance of the ceramics. Photoluminescence (PL) spectra were measured via the spectrofluorometer (FluoroMax-4). The crystal structure for the samples at room temperature was recorded via X-ray diffraction (XRD) analysis (Rigaku Ultima III). The surface/cross-section and distribution of elements for the ceramics were measured by field emission scanning electron microscopy (FESEM, Zeiss Supra 55, Germany) and EDS (Oxford X-Max50), respectively. In addition, 350 grains were randomly selected from the SEM micrographs using the “Nano Measurer” software to determine the average grain size and corresponding distribution. Density was recorded according to the Archimedes method. After polarization with a DC electric field ( $20\text{--}30\text{ kV cm}^{-1}$ ) at  $90^\circ\text{C}$ , the piezoelectric coefficient ( $d_{33}$ ) was measured at room temperature by the quasi-static  $d_{33}$  meter (ZJ-6A, Institute of Acoustics, China). Polarization ( $P$ - $E$ ) and strain ( $S$ - $E$ ) hysteresis loops were measured using a ferroelectric test system (Precision Premier II) at 10 Hz. The temperature dependence of the dielectric constant was measured using the Agilent E4980A LCR meter and the Keithley 2410 Source Meter. Piezoelectric response force microscopy (PFM, Dimension Icon, Bruker, United States) was used to observe the morphology and switching behaviors of the ferroelectric domains. The integrated linear motor (R-LP4, China) was used to perform the force sensitivity test, and the loading force, frequency, and stimulating distance were controlled by computer software. The output current, resistance, voltage, and charge were acquired using the Keithley 2400 SourceMeter and the Keithley 6514 electrometer. It is worth noting that both surfaces of the sample are treated with silver or transparent ITO electrodes before testing for all electrical properties. In addition, when testing the force sensitivity, two wires need to be connected on both surfaces of the sample and wrapped with polyimide tape.

**Simulation method:** For accurate band structure simulations, density functional theory (DFT) simulations were performed via the Vienna ab initio simulation package (VASP) in combination with the projector augmented-wave (PAW) pseudopotentials of generalized gradient approximations (GGA) in the Perdew-Burke-Ernzerhof (PBE) functional form. The modified shell-GGA-1/2 (shGGA-1/2) was introduced for electronic structure calculations to conquer the inherent band gap underestimation problem of DFT. To closely simulate the dopant atoms (i.e., Sm) and 1:1 randomly occupations of K/Na atoms at the A site in KNN, a  $4 \times 4 \times 3$  orthorhombic-phase  $\text{ABO}_3$  supercell including 240 atoms was built by using the special quasi-random structure (SQS). The GPU-accelerated VASP was used for all the calculations, and the  $\Gamma$  centered  $2 \times 2 \times 3$  K-point set and 600 eV cutoff energy were chosen. Meanwhile, the relaxation

convergence for ions and electrons was  $1 \times 10^{-5}$  and  $1 \times 10^{-6}$  eV, respectively. In addition, the self-energy correction was carried out on O anions, with a self-energy potential derived from  $V(\text{O}: 2s^2 2p^4) - V(\text{O}: 2s^2 2p^{3.5})$ , where a cutoff radius of 2.8 Bohr was determined through the variational principle<sup>[5,23-25]</sup>.

## RESULTS AND DISCUSSION

### Transparency of the xSm ceramics

Figure 2A shows the photos of the investigated samples that have been thinned and polished to  $\sim 0.3$  mm. It can be noticed that with the increase in Sm, the milky white opaque pure KNN ceramic gradually turns into yellowish transparent ceramics. When  $1 \leq x \leq 2$ , the font at the bottom and even distant objects can be clearly observed through the xSm ceramics, especially in 2Sm, exhibiting the “window” feature. By conducting the optical transmittance ( $T$ ) tests [Figure 2B], it can be found that the  $T$  of xSm ceramics gradually improves and then deteriorates with the increase in Sm, which is in accordance with the naked eye observation. When  $1 \leq x \leq 2$ , the optical transmittance is greater than 65% in the near-IR region ( $\sim 900$  nm), which is comparable to the reported high transparency KNN-based ceramics<sup>[15,26,27]</sup>. In the optical transmittances ( $T$ ) versus wavelength of the xSm ceramics, it can also be clearly observed that several absorption peaks are concentrated at  $\sim 407$ ,  $\sim 422$ ,  $\sim 464$ , and  $\sim 480$  nm. These peaks are caused by  ${}^6\text{H}_{5/2} \rightarrow {}^4\text{F}_{7/2}$ ,  ${}^6\text{H}_{5/2} \rightarrow {}^4\text{F}_{9/2}$ ,  ${}^6\text{H}_{5/2} \rightarrow {}^6\text{P}_{5/2}$ ,  ${}^6\text{H}_{5/2} \rightarrow {}^4\text{H}_{11/2}$  electronic transitions of  $\text{Sm}^{3+}$ , respectively, so the absorption peaks become more pronounced with the increase in Sm [Figure 2B and C]<sup>[28,29]</sup>. Several excitation peaks corresponding to these transitions can also be observed from the photoluminescence excitation (PLE) spectra monitored at 597 nm, with the strongest excitation peak at  $\sim 407$  nm [Figure 2C]. Therefore, the xSm ceramics exhibit good down-conversion photoluminescence (PL) under excitation at 407 nm, and sharp characteristic green (563 nm), yellow (597 nm), and red (645 nm) emission bands of  $\text{Sm}^{3+}$  can be observed [Figure 2D], and the corresponding PL mechanism is shown in detail in Figure 2E<sup>[30]</sup>.

On the other hand, due to the absorption generated by the interband transition of electrons from the valence band to the conduction band, the optical transmittance of the xSm ceramics begins to drop to zero when it is less than  $\sim 400$  nm [Figure 2B]<sup>[26]</sup>. For KNN-based ceramics, the band gap ( $E_g$ ) is defined as the transition from the top of the valence bands occupied by the  $\text{O}_{2p}$  electron state to the bottom of the conduction bands dominated by the empty  $\text{Nb}_{4d}$  electron state. A smaller  $E_g$  facilitates electronic transitions and reduces the energy used for light transport, leading to greater light losses and poorer optical transmittance. Therefore, the  $E_g$  plays a crucial role in transparency, which can be evaluated based on the Tauc equation according to the absorption band (at  $\sim 400$  nm) for the optical transmittance spectra [Figure 2B]<sup>[5,31]</sup>. As shown in Figure 2F, the fitted  $E_g$  value of the xSm ceramics increases with Sm doping until  $x = 2$ , indicating that appropriate Sm doping is beneficial for improving the optical transmittance in terms of bandgap. In order to theoretically understand the influence of Sm doping on  $E_g$ , we further used the modified shell-GGA-1/2 (shGGA-1/2) method for the calculation of the bandgap of Sm-doped KNN ceramics. Supplementary Figure 1A and B shows the SQS structure of the KNN  $4 \times 4 \times 3$  supercell including 240 atoms and the unfolded primitive cell representation of band structures for KNN, respectively. It is worth noting that the calculated result for shGGA-1/2 bandgap of pure KNN ( $\sim 2.85$  eV) is close to the reported experimental values, indicating that this method is suitable for the bandgap calculation of KNN-based materials<sup>[31,32]</sup>. Since vacancy-related defects are inevitable in the process of heterovalent donor doping for KNN-based ceramics, we considered four cases in the calculation of the bandgap of 2% Sm-doped KNN: without vacancy, with K vacancy, with Na vacancy, and with O vacancy, respectively. As can be seen, the shGGA-1/2 bandgap of the four types of 2% Sm-doped KNN calculated are greater than those of pure KNN to varying degrees [Supplementary Figure 1C], which further indicates that the improvement of  $E_g$  is caused by the doping of Sm in KNN matrix.



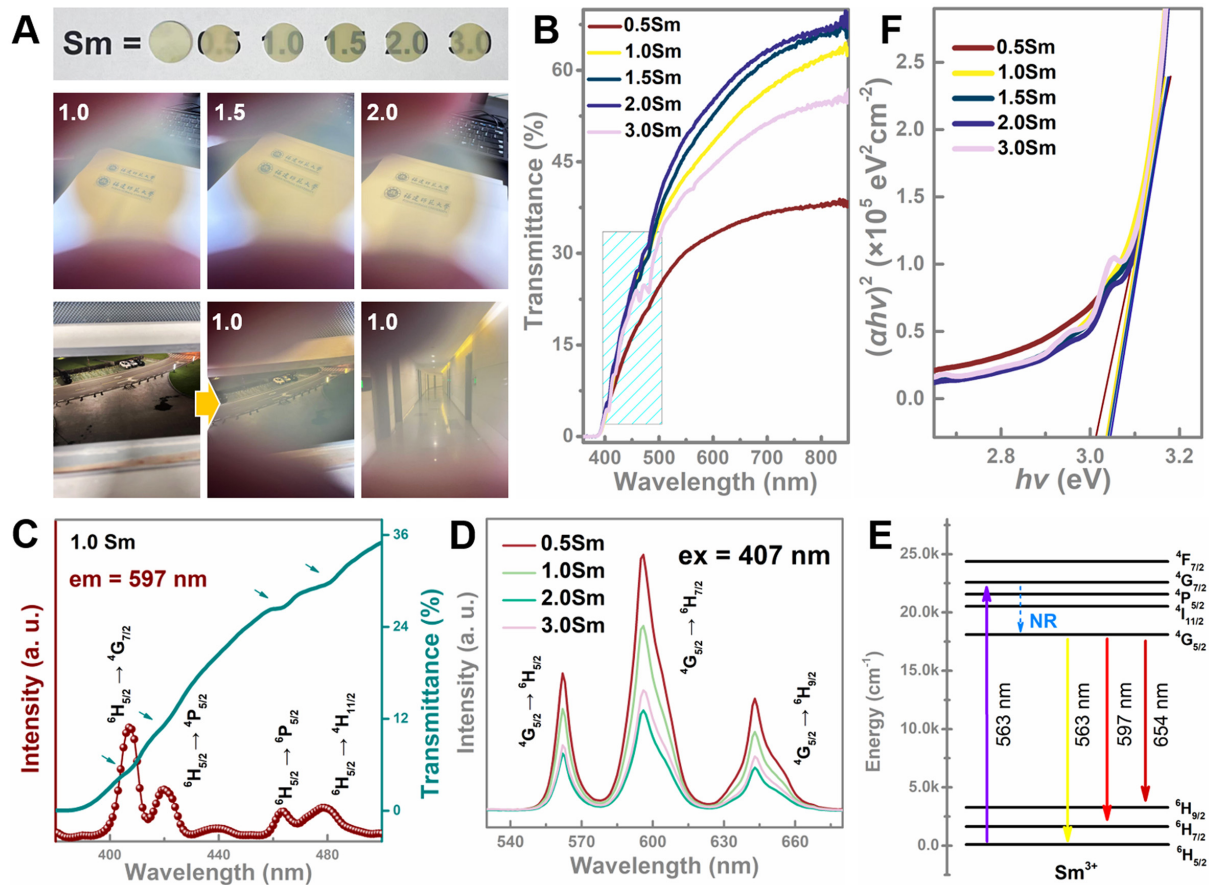


**Figure 2.** (A) Photographs and (B) optical transmittance spectra of the  $x\text{Sm}$  transparent ceramics with a thickness of  $\sim 0.3$  mm. (C) The optical transmittance spectra and photoluminescence excitation spectra monitored at 597 nm of the 1.0 Sm ceramic. (D) The photoluminescence emission spectra excitation at 407 nm of the  $x\text{Sm}$  ceramics. (E) The schematic energy level diagram of  $\text{Sm}^{3+}$ . (F) The plots of  $(h\nu)^2$  versus  $h\nu$  of the  $x\text{Sm}$  transparent ceramics.

### Microstructure of the $x\text{Sm}$ transparent ceramics

In addition to the optical bandgap, the superior transparency of the  $x\text{Sm}$  ceramics is also closely related to their microstructure. The SEM micrographs of the surface/cross-section for the  $x\text{Sm}$  ceramics are shown in Figure 3A–C and Supplementary Figure 2. Appropriate increase in Sm content not only reduces the porosity of the  $x\text{Sm}$  ceramics, but also significantly refines the grain size and improves the corresponding homogeneity. In addition, remarkable transgranular fracture characteristics can be reflected in the cross-section of the  $x\text{Sm}$  ceramics with fine grains ( $x \geq 1$ ), indicating high compactness and excellent mechanical properties [Figure 3B1,C2 and Supplementary Figure 2A1,C1]. The relative density of the  $x\text{Sm}$  ceramics with  $x \geq 1$  can reach  $\geq 97.5\%$  [Supplementary Table 1]. Meanwhile, the uniform element distribution can also be observed in the samples doped with appropriate Sm from the EDS analysis [Figure 3D and Supplementary Figure 3]. According to the statistical analysis results, the average grain size of the  $x\text{Sm}$  ceramics is less than 260 nm when  $x \geq 1$ , much smaller than the wavelength range of visible light (400–780 nm) [Supplementary Figure 4]. Therefore, in addition to reducing light scattering losses with a dense structure, grain sizes smaller than the visible light scattering center can also effectively avoid light scattering, both contributing to the improvement of transparency for the KNN ceramics<sup>[33]</sup>. The refinement of grain size is closely related to vacancy-related defects produced by donor doping<sup>[5]</sup>. When the A-site ions ( $\text{K}^+/\text{Na}^+$ ) in the KNN matrix are replaced by the  $\text{Sm}^{3+}$  with higher valence, the cation vacancies (e.g.,  $V_{\text{Na}}$  or  $V_{\text{K}}$ ) are inevitably generated to balance the charge. Typically, these vacancies tend to concentrate near grain

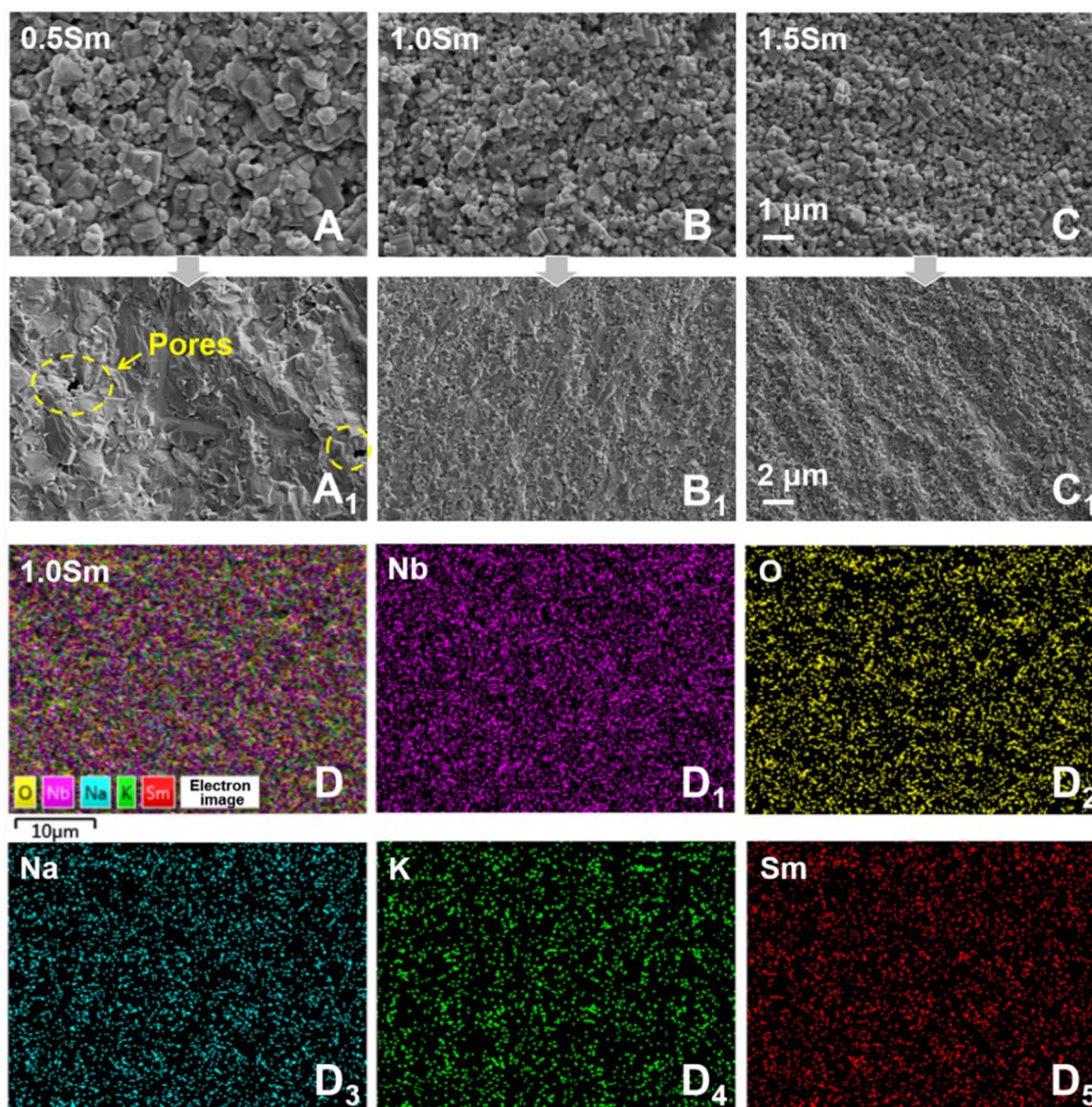


**Figure 3.** (A-C) The free and (A<sub>1</sub>-C<sub>1</sub>) fracture surface of the *x*Sm transparent ceramics. (D) EDS elemental analysis via the SEM micrographs of the 1.0 Sm transparent ceramic.

boundaries with low energy and restrict their mobility, ultimately leading to grain boundary pinning and inhibiting grain growth. However, the doping content of Sm cannot be infinitely increased. When  $x \geq 2.5$ , obvious rod-shaped grains begin to appear inside the ceramic and become more prominent in the 3.0 Sm ceramic, which is the direct reason for the deterioration of transparency [Supplementary Figure 2]. By EDS analysis, it can be found that the content of Sm and K in these rod-shaped impurities is higher than that in the matrix, while the content of K in the matrix was significantly less than that of Na as in other components without rod-shaped grains (e.g.,  $x = 1, 2$ ) [Supplementary Figure 5], which will be further discussed below.

Figure 4A displays the XRD patterns for the *x*Sm ceramics. Several main peak positions of the *x*Sm ceramics are consistent with the PDF card (#77-0038) of pure KNN ceramics, indicating that the doped Sm<sup>3+</sup> has been



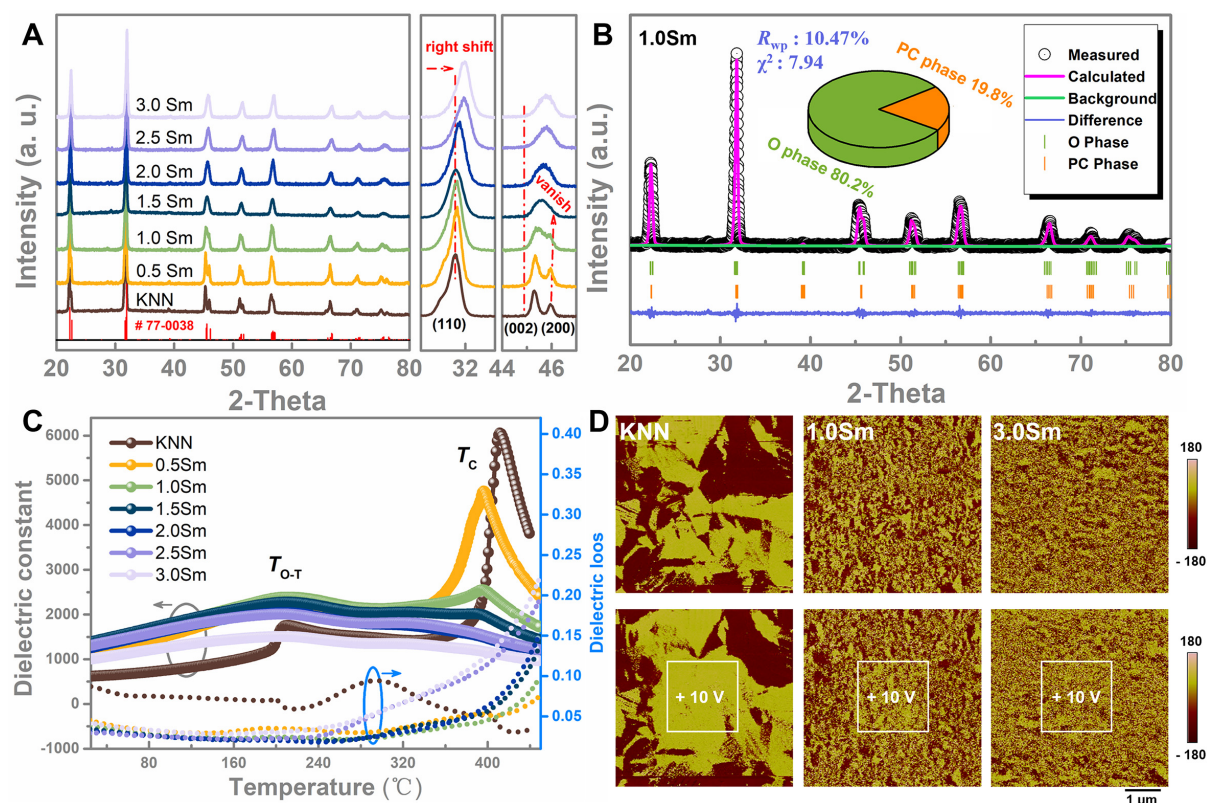


**Figure 4.** (A) XRD patterns of the  $x\text{Sm}$  ceramics. (B) Rietveld refinements for the 1.0 Sm ceramic. (C) Temperature-dependent dielectric constant and loss curves of the  $x\text{Sm}$  ceramics. (D) PFM phase images of the  $x\text{Sm}$  ceramics without and with +10 V DC tip biases applied.

incorporated into the KNN matrix. Due to the A-site ions with large ionic radii ( $\text{K}^+$ :  $1.64 \text{ \AA}/\text{CN} = 12$ ,  $\text{Na}^+$ :  $1.39 \text{ \AA}/\text{CN} = 12$ ) are replaced by the  $\text{Sm}^{3+}$  ions with small ionic radii ( $1.24 \text{ \AA}/\text{CN} = 12$ ), lattice shrinkage occurred. As a result, the diffraction peaks of  $x\text{Sm}$  ceramics tend to shift to higher angles as  $x$  increases. Meanwhile, lattice shrinkage can also force the atomic spacing to shorten, inducing changes in bond angles/lengths and suppressing ferroelectric distortion in the low-symmetry phase, leading to the phase transition. From the split (002)/(200) diffraction peaks near  $2\theta \sim 45^\circ$ , it can be observed that the (200) peak gradually disappears with the increase of  $x$  and eventually forms a unimodal peak, which indicates that the introduction of Sm gradually induces the formation of highly symmetric pseudo-cubic phase, labeled as the PC phase<sup>[31,34]</sup>. Due to the high optical symmetry of the pseudo-cubic phase, its increased content also helps to improve the optical transmittance. Further analysis of the Rietveld refinement results of XRD patterns shows that compared with pure KNN ceramics with a single orthorhombic phase, the proportion of pseudo-cubic phase in the 1.0 Sm sample is increased to 19.8%, and when  $x \geq 2$ , it becomes a single pseudo-cubic phase [Figure 4B and Supplementary Figure 6]. In fact, when sintered under high-temperature conditions (e.g.,  $> 1,100^\circ\text{C}$ ), alkali metal ions (especially K) are prone to evaporate in KNN-based ceramics, so weak second phase ( $\text{K}_6\text{Nb}_{10.8}\text{O}_{30}$ , PDF#32-0821) can be detected in the range of  $2\theta \sim 24\text{--}30^\circ$  when  $x \leq 2$ , which has also been reported previously<sup>[5,27,35]</sup>. When the doping content of Sm is greater than 2%, the excess Sm will react with  $\text{K}_6\text{Nb}_{10.8}\text{O}_{30}$  to further generate the new rod-shaped  $\text{K}_2\text{SmNb}_5\text{O}_{15}$  impurity phase (PDF#39-1441), as shown in Supplementary Figure 2, which seriously affects the transparency of ceramics. Overall, an appropriate amount of Sm doping leads to an increase in the bandgap, density, and pseudo-cubic phase of KNN ceramics, as well as a significant reduction in grain size, resulting in high transparency of the  $x\text{Sm}$  ceramics (i.e.,  $1 \leq x \leq 2$ ).

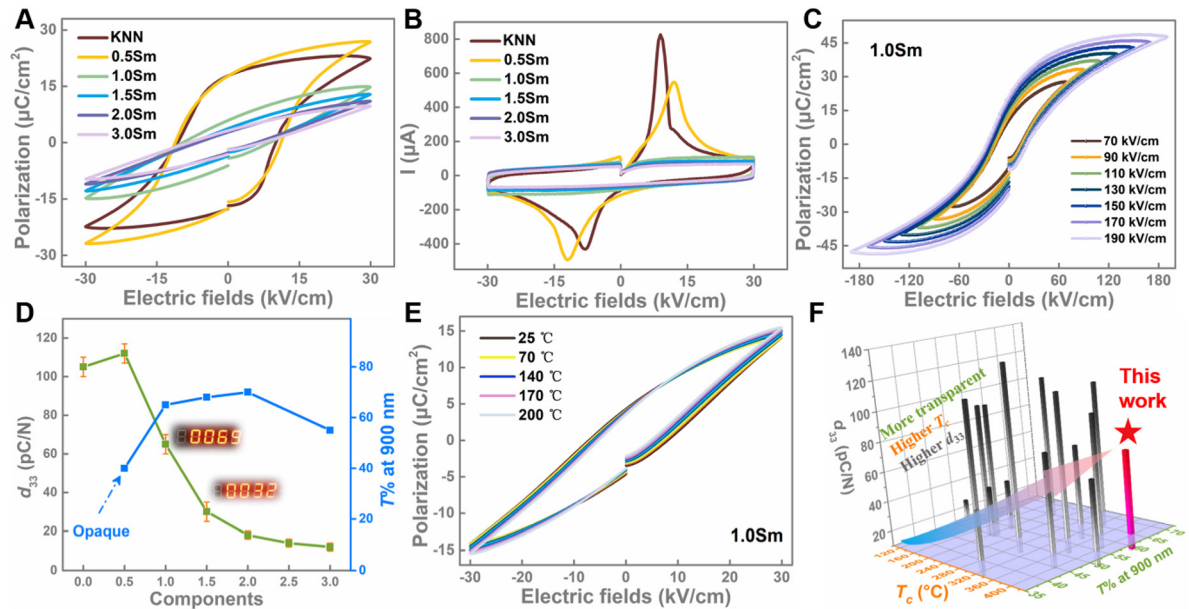


Figure 4C displays the dielectric constant and dielectric loss as a function of the temperature of the  $x$ Sm ceramics recorded at 10 kHz. Two peaks can be seen in all ceramics corresponding to the phase transitions from the orthorhombic to tetragonal phase ( $T_{O-T}$ ) and from the tetragonal to cubic phase ( $T_C$ ), respectively. When the content of Sm increases, the position of dielectric peaks in the  $x$ Sm ceramics does not change obviously (especially  $T_{O-T}$ ), but the diffusion characteristics become more pronounced, indicating enhanced relaxor behavior and weakened ferroelectricity. Meanwhile, the doping of Sm also significantly reduces the dielectric loss, which originates from the improvement of the microstructure density [Figure 3B1,C2 and Supplementary Figure 2A1,C1]. The local information of ferroelectric domain structure was observed using PFM, as displayed in Figure 4D. Because of the direct proportionality between grain size and domain size, the typical orthorhombic bulk microdomains of the KNN ceramics are gradually decomposed into nanodomains as Sm increases. In addition, the formation of nanodomains is also related to the formation of a weakly polar pseudo-cubic phase. To verify the authenticity of the domain signal, a significant domain switching behavior can be observed after applying a +10V DC tip bias to the central region ( $2 \times 2 \mu\text{m}^2$ ) of phase images for PFM. However, compared with pure KNN ceramics, the domains in the 1.0 and 3.0 Sm samples do not switch completely under the applied voltage, further illustrating the enhanced relaxor behavior, which is closely related to the reduction in grain size and lattice volume<sup>[31,36,37]</sup>.

### Ferro/piezoelectricity of the $x$ Sm transparent ceramics

$P$ - $E$  loops of the  $x$ Sm ceramics were tested at room temperature and 10 Hz, as shown in Figure 5A. It is evident that all ceramics exhibit a typical  $P$ - $E$  loop, and as  $x$  increases, the ferroelectric properties of the  $x$ Sm ceramics first increase and then decrease. When  $x = 0.5$ , the increase in ferroelectricity (mainly for the  $P_{\text{max}}$ ) is due, on the one hand, to the increase in densification and, on the other hand, to the improvement of local heterogeneity caused by the formation of phase coexistence induced by trace Sm doping<sup>[38]</sup>. Both aspects improve the room temperature dielectric response, thereby enhancing the  $P_{\text{max}}$  of 0.5 Sm. When  $1 \leq x \leq 2$ , although the densification and room temperature dielectric constant increase further, the ferroelectric properties deteriorate due to the enhanced relaxor behavior caused by the significant reduction in grain size and lattice volume. Finally, due to the generation of the impurity phase ( $\text{K}_2\text{SmNb}_5\text{O}_{15}$ ) and the decrease in dielectric constant, the ferroelectric properties continue to decline in  $x > 2$ . Moreover, it can also be observed from the  $I$ - $E$  curves that the current peak is significantly suppressed when  $x > 0.5$  [Figure 5B], which further reflects the local nanodomains with low domain wall energy induced by the enhanced relaxor behavior<sup>[30]</sup>. The high breakdown field strength of ferroelectric ceramics depends largely on the fine grain size and high densification<sup>[39]</sup>, so proper doping of Sm significantly increases the breakdown field strength of the  $x$ Sm ceramics from 90 kV/cm ( $x = 0$ ) to 250 kV/cm ( $x = 2.5$ ) [Figure 5C, Supplementary Figure 7A and B]. Then, in the 3.0 Sm sample, the formation of a large number of the impurity phase ( $\text{K}_2\text{SmNb}_5\text{O}_{15}$ ) and the increase in dielectric loss lead to the degradation of the breakdown field strength [Supplementary Figure 7C].

Figure 5D displays the piezoelectric coefficient ( $d_{33}$ ) and optical transmittance at 900 nm of the  $x$ Sm ceramics. The piezoelectric coefficient of the piezoelectric material is typically closely related to the residual polarization and dielectric constant<sup>[40]</sup>, so the  $d_{33}$  of the  $x$ Sm ceramics also increases first and then decreases, and reaches the optimal value in the 0.5 Sm ceramic ( $\sim 112$  pC/N). It is noteworthy that although the piezoelectric coefficient of the  $x$ Sm ceramics decreases at  $x > 0.5$ , it remains at  $\sim 69$  pC/N in the 1.0 Sm transparent ceramic. More importantly, due to the high Curie temperature and enhanced relaxor behavior, the 1.0 Sm ceramic also exhibits excellent high-temperature resistance. For example, both the  $P$ - $E$  loops and bipolar electrical field-induced strain of the 1.0 Sm ceramic are not deteriorated but slightly enhanced when the temperature rises from room temperature to 200 °C [Figure 5E, Supplementary Figure 7D and E], which is conducive to practical application. Compared with other reported KNN-based transparent ceramics<sup>[15,27,33,41–47]</sup>, the 1.0 Sm ceramic exhibits significant competitiveness due to its high optical



**Figure 5.** (A)  $P$ - $E$  hysteresis loops and (B)  $I$ - $E$  curves at 10 Hz of the  $x$ Sm ceramics with a thickness of  $\sim 0.3$  mm. (C)  $P$ - $E$  hysteresis loops under different electric fields at 10 Hz of the 1.0 Sm ceramics with a thickness of  $\sim 0.25$  mm. (D)  $d_{33}$  value and optical transmittance (at  $\sim 900$  nm) of the  $x$ Sm ceramics. (E)  $P$ - $E$  hysteresis loops under different temperatures at 10 Hz of the 1.0 Sm ceramics with a thickness of  $\sim 0.3$  mm. (F) The comprehensive performance comparisons of the 1.0 Sm ceramic with other representative KNN-based transparent ceramics.

transmittance ( $T \sim 65\%$ ,  $\sim 900$  nm), high Curie temperature ( $\sim 395$  °C), and good piezoelectric properties ( $\sim 69$  pC/N) [Figure 5F].

### Force sensitivity of the $x$ Sm transparent ceramics

The environmental protection, intelligence, and multi-functional integration of materials are the trends of science and technology development in the new era. For instance, observation windows in high-pressure environments such as high altitude (e.g., aerospace) or deep sea (e.g., diving) require the use of smart materials that are sensitive to external forces (e.g., piezoelectric transparent ceramics, TPC) to issue timely warnings in overpressure environments [Figure 6A], thereby avoiding damage to personnel and property caused by window rupture, which is not possible with traditional glass windows. Smart windows can be made by integrating TPC in the form of a sandwich inside a high-strength conventional transparent material to act as a transparent force-sensitive layer. For the  $x$ Sm TPC with high Curie temperature, high optical transmittance, and good piezoelectricity, there is potential in this regard, so their pressure sensitive properties were further evaluated. Figure 6B displays the schematic diagram of the experimental apparatus for testing the output piezoelectric current signal; more detailed information can be found in the previous report<sup>[48]</sup>. The piezoelectric effect is a process of electromechanical conversion, and the piezoelectric output signal of the test can be divided into contact, compression, release, and separation of four stages<sup>[48,49]</sup>. It is generally assumed that the durations of contact and separation, as well as compression and release, are equal. In the contact stage, no current flows through the circuit, and this duration is represented as  $aT$  ( $T$  is the time of the entire cycle;  $a$  is related to the stimulus distance: the longer the stimulus distance, the larger  $a$ ). Subsequently, as external force begins to compress the sample, the positive and negative charges separate and accumulate respectively on both sides of the sample. When there is an external circuit, an electric current is generated. After the duration of  $[(1-2a)/2]T$ , the external force reaches its maximum value, and the sample will undergo extreme deformation and produce peak current. Finally, external force begins to be released, generating a reverse peak current with a duration of  $[(1-2a)/2]T$ .

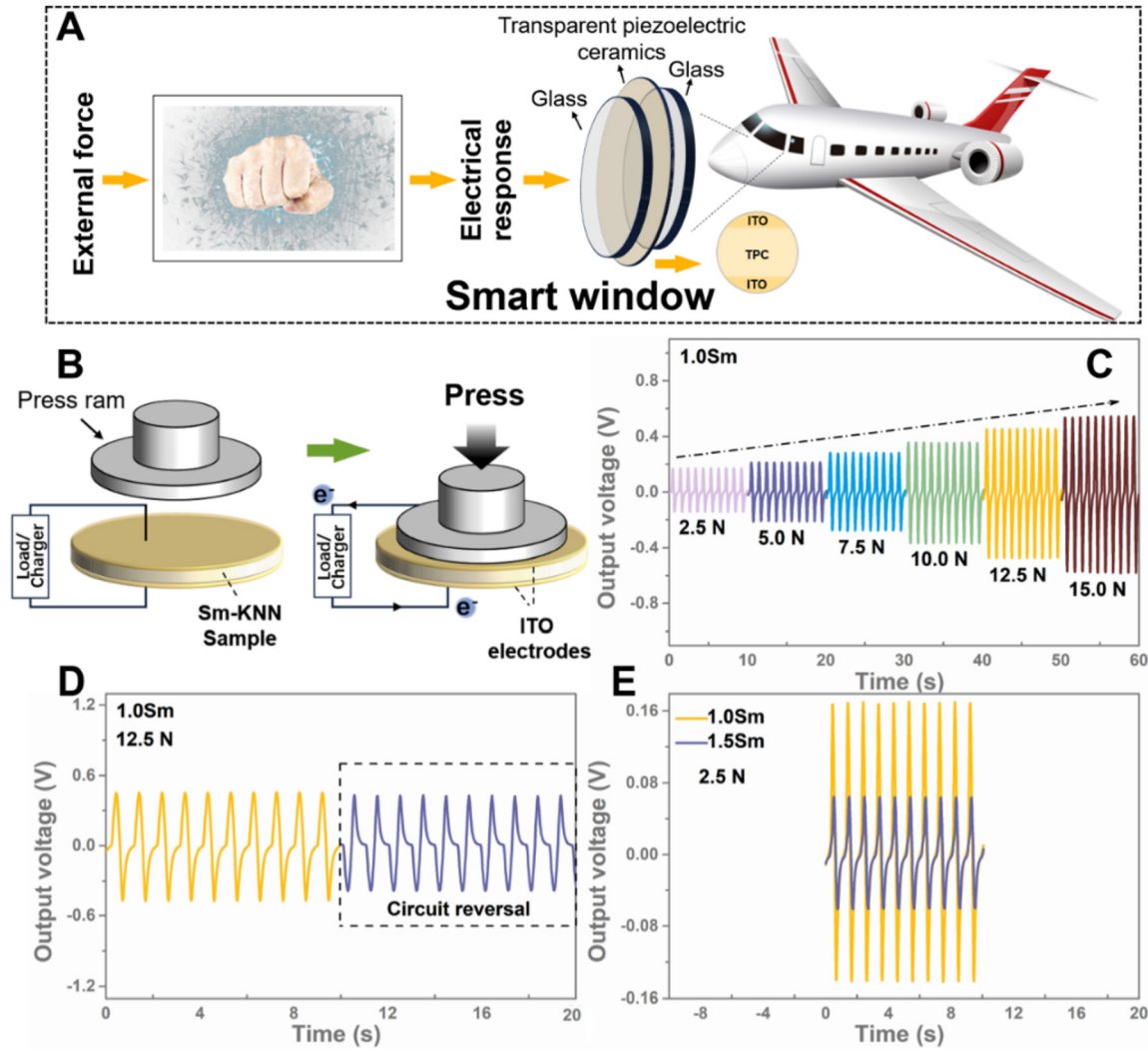


**Figure 6.** (A) The application concept of the piezoelectric transparent ceramics (TPC) in smart windows. (B) The diagram of pressure-electric response test. (C) Output voltage curves of the 1.0 Sm transparent ceramics under different pressures at 1 Hz. (D) The forward and reverse output voltage curves of the 1.0 Sm transparent ceramics under 1 Hz and 12.5 N. (E) The comparisons of the output voltage curves under 1 Hz and 2.5 N for the 1.0 and 1.5 Sm transparent ceramics.

Figure 6C shows the short-circuit voltage variation over time of the 1.0 Sm TPC with different uniaxial pressures and a frequency of 1 Hz. It can be observed that all short-circuit voltage curves exhibit nearly symmetrical positive and negative distributions over time, which is consistent with the response behavior of the opaque BCTH<sub>x</sub> ceramics and commercial PZT-based ceramics. This tendency is not influenced by the forward or reverse connection, as is the short-circuit current [Figure 6D, Supplementary Figure 8A]. This results from the force's loading and unloading times being virtually identical. In addition, larger uniaxial pressures lead to greater deformation and thus more charge. Therefore, the short-circuit voltage of the 1.0 Sm TPC increases as the uniaxial pressure increases, showing excellent force response characteristics. When only 10 N of force is applied, the short-circuit voltage of the 1.0 Sm TPC can reach ~0.34 V and exhibit excellent cyclic characteristics [Figure 6C, Supplementary Figure 8B]. It is worth noting that due to the low  $d_{33}$  of the 1.5 Sm TPC, its short-circuit voltage is discounted [Figure 6E]. The prominent force-sensitive properties further illustrate the application potential of the 1.0 Sm TPC in smart windows.



## CONCLUSIONS

In summary, the transparent KNN-based ferro/piezoelectric ceramics (abbreviated as  $x\text{Sm}$ ) were developed based on simple single rare earth doping combined with traditional solid-state reaction method, which can be used for smart windows with superior force-sensitive properties by using piezoelectric effect. Through multidimensional microstructure analysis, it was found that proper  $\text{Sm}^{3+}$  doping induced finer grain size, higher densification and bandgap, and more pseudo-cubic phase, effectively reducing the incident light loss caused by the central scattering and optical anisotropy, thereby improving the optical transmittance. When  $1 \leq x \leq 2$ , the optical transmittance is greater than ~65% at ~900 nm. As the Sm content further increased, the appearance of the impurity phase and the decrease in densification did not lead to a further increase in the optical transmittance. On the other hand, the doping of Sm also leads to the enhancement of relaxor behavior, resulting in the deterioration of piezoelectricity. Despite this, the 1.0 Sm ceramic still maintains good piezoelectricity. More importantly, due to the small degree of doping, the Curie temperature of KNN ceramics did not decrease significantly. High optical transmittance (~65%, 900 nm), high Curie temperature (~395 °C), and good piezoelectricity (~65 pC/N) make the 1.0 Sm ceramic competitive among KNN-based transparent ceramics. Interestingly, based on the force-sensitive testing, it was found that the 1.0 Sm ceramic produces excellent electrical signal output (~0.34 V) under low force action (10 N), and good cycling, which has great potential in the application of smart windows.

## DECLARATIONS

### Authors' contributions

The conception and design of the work: Lin, J.; Li, P.; Yang, Z.

The acquisition and analysis of data: Lin, J.; Peng, J.; Huang, X.; Lin, Q.; Wu, X.

The interpretation of data: Lin, J.; Peng, J.; Lin, Q.

The writing and revising: Lin, J.; Peng, J.

The supervision: Li, P.; Yang, Z.

### Availability of data and materials

The raw data are listed in the [Supplementary Materials](#). Further data used to support the findings of this study are available from the corresponding authors upon reasonable request.

### Financial support and sponsorship

This work was supported by the Fujian Province Young and Middle-aged Teacher Education Research Project (JZ240009) and the Innovation Team of Fujian Normal University (Y07204080K13).

### Conflicts of interest

All authors declared that there are no conflicts of interest.

### Ethical approval and consent to participate

Not applicable.

### Consent for publication

Not applicable.

### Copyright

© The Author(s) 2025.

## REFERENCES

1. Ke, Y.; Chen, J.; Lin, G.; et al. Smart windows: electro-, thermo-, mechano-, photochromics, and beyond. *Adv. Energy. Mater.* **2019**, *9*, 1902066. DOI
2. Ke, Y.; Zhou, C.; Zhou, Y.; Wang, S.; Chan, S. H.; Long, Y. Emerging thermal-responsive materials and integrated techniques targeting the energy-efficient smart window application. *Adv. Funct. Mater.* **2018**, *28*, 1800113. DOI
3. Chen, X.; Luo, L.; Zeng, Z.; et al. Bio-inspired flexible vibration visualization sensor based on piezo-electrochromic effect. *J. Materiomics.* **2020**, *6*, 643-50. DOI
4. Kim, K.; Jeong, S.; Koo, B.; Ahn, H. Surface amending effect of N-doped carbon-embedded NiO films for multirole electrochromic energy-storage devices. *Appl. Surf. Sci.* **2021**, *537*, 147902. DOI
5. Wu, X.; Lin, J.; Xu, Z.; et al. Defect management and multi-mode optoelectronic manipulations via photo-thermochromism in smart windows. *Laser. Photonics. Rev.* **2021**, *15*, 2100211. DOI
6. Li, J.; Qu, W.; Daniels, J.; et al. Lead zirconate titanate ceramics with aligned crystallite grains. *Science* **2023**, *380*, 87-93. DOI
7. Wang, L. V.; Yao, J. A practical guide to photoacoustic tomography in the life sciences. *Nat. Methods.* **2016**, *13*, 627-38. DOI PubMed PMC
8. Yan, P.; Qin, Y.; Xu, Z.; et al. H Highly transparent Eu-doped 0.72PMN-0.28PT ceramics with excellent piezoelectricity. *ACS. Appl. Mater. Interfaces.* **2021**, *13*, 54210-6. DOI
9. Gao, X.; Qiao, L.; Qiu, C.; et al. A robust, low-voltage driven millirobot based on transparent ferroelectric crystals. *Appl. Phys. Lett.* **2022**, *120*, 032902. DOI
10. Fang, Z.; Jiang, X.; Tian, X.; et al. Ultratransparent PMN-PT electro-optic ceramics and its application in optical communication. *Adv. Opt. Mater.* **2021**, *9*, 2002139. DOI
11. Deng, C.; Ye, L.; He, C.; et al. Reporting excellent transverse piezoelectric and electro-optic effects in transparent rhombohedral PMN-PT single crystal by engineered domains. *Adv. Mater.* **2021**, *33*, e2103013. DOI
12. Sun, E.; Cao, W. Relaxor-based ferroelectric single crystals: growth, domain engineering, characterization and applications. *Prog. Mater. Sci.* **2014**, *65*, 124-210. DOI PubMed PMC
13. Qiu, C.; Wang, B.; Zhang, N.; et al. Transparent ferroelectric crystals with ultrahigh piezoelectricity. *Nature* **2020**, *577*, 350-4. DOI
14. Huangfu, G.; Zeng, K.; Wang, B.; et al. Giant electric field-induced strain in lead-free piezoceramics. *Science* **2022**, *378*, 1125-30. DOI
15. Lin, J.; Wang, Y.; Xiong, R.; et al. Tailoring micro-structure of eco-friendly temperature-insensitive transparent ceramics achieving superior piezoelectricity. *Acta. Mater.* **2022**, *235*, 118061. DOI
16. Ren, X.; Peng, Z.; Chen, B.; et al. A compromise between piezoelectricity and transparency in KNN-based ceramics: the dual functions of Li<sub>2</sub>O addition. *J. Eur. Ceram. Soc.* **2020**, *40*, 2331-7. DOI
17. Ren, X.; Chai, Q.; Zhao, X.; et al. Relaxor behaviors and electric response in transparent 0. *Ceram. Int.* **2019**, *45*, 3961-8. DOI
18. Kosec, M.; Bobnar, V.; Hrovat, M.; Bernard, J.; Malic, B.; Holc, J. New lead-free relaxors based on the K<sub>0.5</sub>Na<sub>0.5</sub>NbO<sub>3</sub>-SrTiO<sub>3</sub> solid solution. *J. Mater. Res.* **2004**, *19*, 1849-54. DOI
19. Du, H.; Zhou, W.; Zhu, D.; et al. Sintering characteristic, microstructure, and dielectric relaxor behavior of (K<sub>0.5</sub>Na<sub>0.5</sub>)NbO<sub>3</sub>-(Bi<sub>0.5</sub>Na<sub>0.5</sub>)TiO<sub>3</sub> lead-free ceramics. *J. Am. Ceram. Soc.* **2008**, *91*, 2903-9. DOI
20. Li, F.; Kwok, K.; Gupta, S. K<sub>0.5</sub>Na<sub>0.5</sub>NbO<sub>3</sub>-based lead-free transparent electro-optic ceramics prepared by pressureless sintering. *J. Am. Ceram. Soc.* **2013**, *96*, 3557-62. DOI
21. Li, F.; Kwok, K. Fabrication of transparent electro-optic (K<sub>0.5</sub>Na<sub>0.5</sub>)<sub>1-x</sub>Li<sub>x</sub>Nb<sub>1-x</sub>Bi<sub>x</sub>O<sub>3</sub> lead-free ceramics. *J. Eur. Ceram. Soc.* **2013**, *33*, 123-30. DOI
22. Qu, B.; Du, H.; Yang, Z. Lead-free relaxor ferroelectric ceramics with high optical transparency and energy storage ability. *J. Mater. Chem. C.* **2016**, *4*, 1795-803. DOI
23. Hutchinson, M.; Widom, M. VASP on a GPU: application to exact-exchange calculations of the stability of elemental boron. *Comput. Phys. Commun.* **2012**, *183*, 1422-6. DOI
24. Hacene, M.; Anciaux-Sedrakian, A.; Rozanska, X.; Klahr, D.; Guignon, T.; Fleurat-Lessard, P. Accelerating VASP electronic structure calculations using graphic processing units. *J. Comput. Chem.* **2012**, *33*, 2581-9. DOI PubMed
25. Liu, C.; Wang, Q.; Wu, X.; et al. Boosting upconversion photoluminescence and multielectrical properties via er-doping-modulated vacancy control in Ba<sub>0.85</sub>Ca<sub>0.15</sub>Ti<sub>0.9</sub>Zr<sub>0.1</sub>O<sub>3</sub>. *ACS. Omega.* **2019**, *4*, 11004-13. DOI
26. Dai, Z.; Li, D.; Zhou, Z.; et al. A strategy for high performance of energy storage and transparency in KNN-based ferroelectric ceramics. *Chem. Eng. J.* **2022**, *427*, 131959. DOI
27. Rahman, A.; Park, S.; Min, Y.; et al. An easy approach to obtain large piezoelectric constant in high-quality transparent ceramics by normal sintering process in modified potassium sodium niobate ceramics. *J. Eur. Ceram. Soc.* **2020**, *40*, 2989-95. DOI
28. Sun, H.; Liu, J.; Wang, X.; Zhang, Q.; Hao, X.; An, S. (K,Na)NbO<sub>3</sub> ferroelectrics: A new class of solid-state photochromic materials with reversible luminescence switching behavior. *J. Mater. Chem. C.* **2017**, *5*, 9080-7. DOI
29. Zhang, Q.; Chen, K.; Wang, L.; Sun, H.; Wang, X.; Hao, X. A highly efficient, orange light-emitting (K<sub>0.5</sub>Na<sub>0.5</sub>)NbO<sub>3</sub>:Sm<sup>3+</sup>/Zr<sup>4+</sup> lead-free piezoelectric material with superior water resistance behavior. *J. Mater. Chem. C.* **2015**, *3*, 5275-84. DOI
30. Qiao, X.; Sheng, A.; Wu, D.; et al. A novel multifunctional ceramic with photoluminescence and outstanding energy storage properties. *Chem. Eng. J.* **2021**, *408*, 127368. DOI

31. Yang, D.; Yang, Z.; Zhang, X.; Wei, L.; Chao, X.; Yang, Z. High transmittance in lead-free lanthanum modified potassium-sodium niobate ceramics. *J. Alloy. Compd.* **2017**, *716*, 21-9. [DOI](#)
32. Chao, X.; Ren, X.; Zhang, X.; et al. Excellent optical transparency of potassium-sodium niobate-based lead-free relaxor ceramics induced by fine grains. *J. Eur. Ceram. Soc.* **2019**, *39*, 3684-92. [DOI](#)
33. Zhao, X.; Chao, X.; Wu, D.; Liang, P.; Yang, Z. Simultaneous realization of high transparency and piezoelectricity in low symmetry KNN-based ceramics. *J. Am. Ceram. Soc.* **2019**, *102*, 3498-509. [DOI](#)
34. Liu, H.; Wang, J.; Wang, H.; Xu, J.; Zhou, C.; Qiu, W.  $\text{Er}^{3+}$  and  $\text{Sr}(\text{Bi}_{0.5}\text{Nb}_{0.5})\text{O}_3$ -modified  $(\text{K}_{0.5}\text{Na}_{0.5})\text{NbO}_3$ : a new transparent fluorescent ferroelectric ceramic with high light transmittance and good luminescence performance. *Ceram. Int.* **2022**, *48*, 4230-7. [DOI](#)
35. Cheng, L.; Wang, K.; Yao, F.; Zhu, F.; Li, J.; Zhang, S. Composition inhomogeneity due to alkaline volatilization in Li-modified  $(\text{K}, \text{Na})\text{NbO}_3$  lead-free piezoceramics. *J. Am. Ceram. Soc.* **2013**, *96*, 2693-5. [DOI](#)
36. Yang, W.; Li, P.; Wu, S.; Li, F.; Shen, B.; Zhai, J. A study on the relationship between grain size and electrical properties in  $(\text{K}, \text{Na})\text{NbO}_3$ -based lead-free piezoelectric ceramics. *Adv. Elect. Mater.* **2019**, *5*, 1900570. [DOI](#)
37. Ren, X.; Jin, L.; Peng, Z.; et al. Regulation of energy density and efficiency in transparent ceramics by grain refinement. *Chem. Eng. J.* **2020**, *390*, 124566. [DOI](#)
38. Pinho, R.; Tkach, A.; Zlotnik, S.; et al. Spark plasma texturing: a strategy to enhance the electro-mechanical properties of lead-free potassium sodium niobate ceramics. *Appl. Mater. Today.* **2020**, *19*, 100566. [DOI](#)
39. Yang, Z.; Du, H.; Qu, S.; et al. Significantly enhanced recoverable energy storage density in potassium-sodium niobate-based lead free ceramics. *J. Mater. Chem. A.* **2016**, *4*, 13778-85. [DOI](#)
40. Li, P.; Fu, Z.; Wang, F.; et al. High piezoelectricity and stable output in  $\text{BaHfO}_3$  and  $(\text{Bi}_{0.5}\text{Na}_{0.5})\text{ZrO}_3$  modified  $(\text{K}_{0.5}\text{Na}_{0.5})(\text{Nb}_{0.96}\text{Sb}_{0.04})\text{O}_3$  textured ceramics. *Acta. Mater.* **2020**, *199*, 542-50. [DOI](#)
41. Zhang, X.; Yang, D.; Yang, Z.; et al. Transparency of  $\text{K}_{0.5}\text{Na}_{0.5}\text{NbO}_3$ - $\text{Sr}(\text{Mg}_{1/3}\text{Nb}_{2/3})\text{O}_3$  lead-free ceramics modulated by relaxor behavior and grain size. *Ceram. Int.* **2016**, *42*, 17963-71. [DOI](#)
42. Yang, D.; Ma, C.; Yang, Z.; et al. Optical and electrical properties of pressureless sintered transparent  $(\text{K}_{0.37}\text{Na}_{0.63})\text{NbO}_3$ -based ceramics. *Ceram. Int.* **2016**, *42*, 4648-57. [DOI](#)
43. Kwok, K. W.; Li, F.; Lin, D. A novel lead-free transparent ceramic with high electro-optic coefficient. *Funct. Mater. Lett.* **2011**, *4*, 237-40. [DOI](#)
44. Wu, X.; Lu, S.; Kwok, K. Photoluminescence, electro-optic response and piezoelectric properties in pressureless-sintered Er-doped KNN-based transparent ceramics. *J. Alloy. Compd.* **2017**, *695*, 3573-8. [DOI](#)
45. Zhao, X.; Chai, Q.; Chen, B.; Chao, X.; Yang, Z. Improved transmittance and ferroelectric properties realized in KNN ceramics via SAN modification. *J. Am. Ceram. Soc.* **2018**, *101*, 5127-37. [DOI](#)
46. Liu, Y.; Yi, W.; Yan, C.; Ma, J.; Fan, L. A novel transparent material based on KNN ferroelectric ceramics. *Ferroelectrics* **2021**, *573*, 173-8. [DOI](#)
47. Chai, Q.; Zhao, X.; Chao, X.; Yang, Z. Enhanced transmittance and piezoelectricity of transparent  $\text{K}_{0.5}\text{Na}_{0.5}\text{NbO}_3$  ceramics with  $\text{Ca}(\text{Zn}_{1/3}\text{Nb}_{2/3})\text{O}_3$  additives. *RSC. Adv.* **2017**, *7*, 28428-37. [DOI](#)
48. Huang, X.; Dong, G.; Zhang, Y.; et al. Decoding the intrinsic frequency response behaviors of piezoelectric output current toward advanced sensing and monitoring applications. *Nano. Energy.* **2025**, *134*, 110544. [DOI](#)
49. Chen, C.; Zhao, S.; Pan, C.; et al. A method for quantitatively separating the piezoelectric component from the as-received "Piezoelectric" signal. *Nat. Commun.* **2022**, *13*, 1391. [DOI](#) [PubMed](#) [PMC](#)